4-27-2021

Electrostatic levitation: an elegant method to control MEMS switching operation

Mohammad Mousavi
Binghamton University--SUNY, smousav1@binghamton.edu

Mohammad Alzgool
Binghamton University--SUNY, malzgoo1@binghamton.edu

Shahrzad Towfighian
Binghamton University--SUNY, stowfigh@binghamton.edu

Noname manuscript No.
(will be inserted by the editor)

Electrostatic levitation: an elegant method to control MEMS switching operation

Mohammad Mousavi · Mohammad Alzgool · Shahrzad Towfighian

Received: date / Accepted: date

Abstract This paper investigates the characteristics of a micro-switch that uses two side electrodes to open a normally closed switch. The side electrodes surround the fixed electrode in the well-known gap-closing electrode configuration. The side electrodes can open a closed switch and be tuned to respond appropriately to outside forces. The combined electrode system dramatically improves the control of a standard gap-closing electrode configuration. In conventional switches, a DC voltage above a certain value closes the switch. To reopen the switch, the voltage difference is reduced to peel off the moving electrode. Currently the contact area is carefully designed to avoid stiction, but the degradation over time and stiction forces can cause a permanent failure. In this work, opening occurs by feeding the side electrodes a voltage beyond a certain value that results in a levitation force. Even if the degradation in the surfaces happen, the switch can open by increasing the side voltages. The characteristics of the combined actuation system are thoroughly analyzed and include the static pull-in, static displacement, release voltage, dynamic pull-in, frequency response, and basins of attraction. The results are validated by the experimental tests. The levitation-based micro-switch improves the system tunability as the sensitivity and switching thresholds can be adjusted.

Keywords MEMS · RF switch · Dynamics · Nonlinear response · electrostatic levitation force · tunability · potential energy · reliability

Mohammad Mousavi
E-mail: smousav1@binghamton.edu

Mohammad Alzgool
E-mail: malzgoo1@binghamton.edu

Shahrzad Towfighian (Corresponding author)
Tel.: +607-777-5315
E-mail: stowfigh@binghamton.edu
State University of New York at Binghamton
4400 Vestal Parkway
Binghamton, New York 13902

1 Introduction

A considerable part of industry uses micro-electromechanical system (MEMS) sensors and switches as appropriate substitutes to operate electronic devices. Specifically, electrostatically actuated direct-contact micro-switches provide fast driving speeds, controllability, sensitivity, low contact resistance, low insertion loss, wide frequency band [1], high-temperature operation, and easy fabrication process because of the simple actuation design. The standard MEMS fabrication techniques allow for a low-cost mass production. Also, MEMS devices are easily integrated with CMOS wafers [2] which makes them ideal for industrial applications. However, permanent failure and nonlinearities in the actuation process limit their usefulness. The rest of this section reviews issues associated with normally open and closed MEMS switches.

Much research on MEMS switches has concerned the electrostatic attractive force that causes pull-in instability that closes the switch and keeps it closed. The conventional actuation of MEMS devices uses a gap-closing capacitor (Fig. 1). Charging the electrodes generates an electrostatic field that moves the top electrode down to the fixed one. When the actuation voltage exceeds a specific value (called pull-in voltage), the movable electrode loses stability and sticks to the bottom electrode. Conventional actuation relies only on the reduction of voltage to peel off the movable electrode (re-

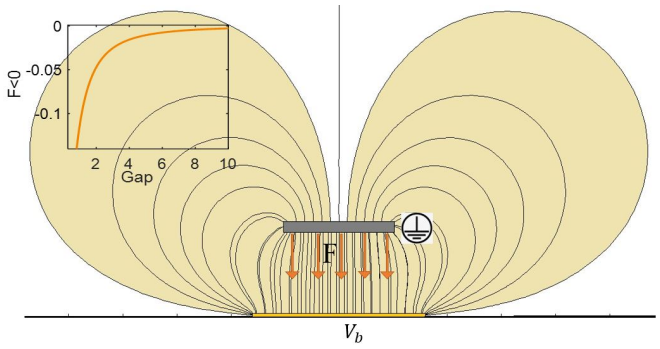

Fig. 1: The electrostatic field of a gap-closing capacitor applies an attractive force to the movable electrode. The electrostatic force per unit length (obtained from COMSOL simulation) is shown in the small figure at the top. Both axes are nondimensional.

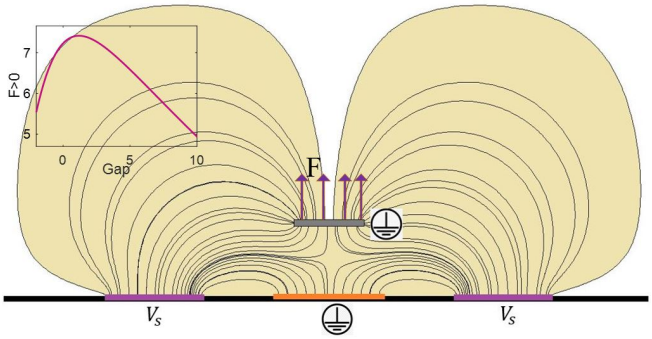

Fig. 2: The electrostatic field in the presence of side electrodes. The electrostatic streams deviate to the sides causing a repulsive force away from the bottom electrode. The electrostatic force per unit length (obtained from COMSOL simulation) is shown in the small figure at the top. Both axes are nondimensional.

open the switch), but any degradation at the contact surfaces can cause a change in the switch characteristics such as a permanent collapse of the switch because of strong surface adhesion forces. Surface erosion occurs at the switch drain spot of the MEMS switches as reported in [3]. Normally open micro-relays repeatedly hit the substrate during the closing process, which accumulates damage through time. As the contact resistance of the drain terminal changes [4,1,5], the switch performance degrades and life shortens.

The fringe-field effect from side electrodes has been introduced as an alternative method to actuate MEMS devices. This methods has been studied for the purpose of avoiding lower substrates [6–8]. Theoretical frameworks have been proposed for a pre-buckled micro-bridge actuated by the fringe-field effect [9,10]. One drawback was that the pre-buckled beam relied on residual stresses that were difficult to control during a microfabrication process. The effect of two side electrodes on the beam dynamics was analytically studied by Kambali and Pandey [11]. Similar to the present work, the configuration included both parallel-plate and side electrodes. They improved the sensitivity and range of operation as a result of the combined side and parallel-plate electrodes. However, the results were not validated by experiments.

Our previous investigations [12–14] offered a supplementary actuation that originates from shielding the bottom surface of the movable electrode and directing the electrostatic field lines to the top surface of movable electrode. This creates a repulsive (levitation) force away from the bottom electrode (Fig. 2). Appending a repulsive supplementary actuation to the typical design provides a more thorough control of the switching operation during opening and closing. Using the levitation force led to the innovation of micro-devices such as pressure sensor, accelerometers [15], micro-mirror [16], MEMS transducers [17] MEMS microphones [18] and MEMS filters [19]. With the addition of the repulsive force to the gap-closing configuration, the combined mechanism enables the creation of innovative MEMS devices as they can be equipped with a bi-directional actuation [14]. Activation of the levitation mechanism can overcome the stiction, and the mechanism can provide better control of the switch.

Normally open switches suffer from bouncing of the movable electrode [20]. The movable electrode mostly fails to stick to the terminal spot once the actuation voltage is applied [21]. This phenomenon happens when a relatively large voltage is applied to the gate and consequently the movable electrode hits the substrate and bounces back. The imperfect actuation can be dangerous or damage the interconnected systems. In this study, we introduce a normally closed switch that is actuated upward (See Figs. 3,4). With the proposed system, we offer a better control of the switch behavior; a control that is not affected by the contact area and geometrical parameters.

Switching time is an important factor in the design of MEMS switches and is defined as how long the opening or closing of a switch takes [22,23]. In many applications such as RF MEMS devices and safety systems, the operation speed is a key factor in the performance analysis. Slow switch response may result in serious injury or equipment damage [23,24]. The opening of conventional gap-closing MEMS switches is relatively slow because the pull-off process is initiated by a reduction of the actuation voltage. With imperfect surfaces or permanent stiction, the switch operates earlier or

later than the specified threshold. The surface force depends on environmental variables such as temperature [2,3,25–31], pressure [26,27] and humidity [25–27].

Conditions that can affect the switching time include the surface interaction forces. The most common surface interaction force is the capillary force, which was investigated theoretically and experimentally by Mastramgelo and Hsu [32]. Later researches include measurement of the adhesion force for s-shaped and arc-shaped micro-cantilever beams in a pulled-in position [33]. Stiction forces such as Capillary and van der Waals forces have been modeled using finite element modeling [34,35]. Because of numerous parameters that can affect the surface forces, empirical approaches are the most reliable ones. In the present work, we will use a theoretical model and experimental data to measure the surface forces during the pull-in position as the bias voltage varies.

The combination of electrostatic levitation and gap-closing mechanisms was introduced in a previous work that enabled tunability [36]. Also, the feasibility of the MEMS switch was shown experimentally in another work [13]. However, there is a lack of knowledge on the fundamental nonlinear behavior of the MEMS switch actuation that combines electrostatic levitation and gap-closing mechanism. This study provides a thorough analysis of the static and dynamic behaviors of the switch by using theoretical and experimental approaches. The opening and closing processes, as well as the switch threshold and system sensitivity are investigated. The introduction is followed by a mechanical description (Section. 2). A model that is consistent with the static and dynamic experiments as well as an energy analysis is provided in the mathematical modeling (Section. 3). Then, in the experimental setup section (Section. 4) we describe the necessary procedures and the apparatus for conducting the tests. In the next two sections, static and dynamic characterizations such as static (SPI) and dynamic pull-in (DPI) voltages, release voltages, equilibrium analyses, time responses, and frequency responses are elaborated. The results are then summarized in Section. 7.

2 Mechanism Description

The switch of interest consists of a micro-cantilever as the movable electrode, a fixed electrode on the substrate below the movable electrode, and two side electrodes one at each side of the bottom electrode. In this paper, the movable electrode is also referred to as a micro-beam or micro-cantilever. As shown in Fig. 1, the well-known gap-closing electrodes produce an attractive force that moves the micro-cantilever to the bottom electrode. When side electrodes are added, they generate a strong electrostatic fringe field that pushes the micro-beam upward, Fig. 2. Repulsive actuation is desirable in micro-sensors and actuators because the actuation direction is not limited by the substrate. This idea is explained by the physical phenomenon Electrostatic Levitation i.e. levitating charged objects in an electrostatic field. Hence, we call the introduced micro-switch 'levitation-based micro-switch'. As the side electrodes are charged, the electrostatic field of the bottom electrode bends to its sides and in the case of applying a sufficiently large side voltage, the resultant force of the compound electrostatic field turns into a repulsive force instead of attractive and the micro-beam is pushed upward. We use repulsive and attractive to mean away from and toward the substrate, respectively.

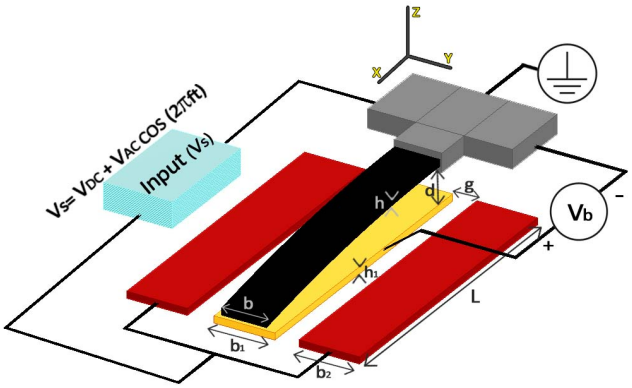

Fig. 3: Levitation-based micro-switch mechanism at ON (initial) state by charging the bottom electrode with a DC voltage. At this state, the side voltage are not charged. The geometric symbols of the design are found in this figure.

As a result of the bottom voltage, the micro-switch is initially in the closed position. In this situation, the micro-beam is pulled-in to the substrate. Dimples are fabricated in the underneath surface of the micro-beam to limit the area of its direct contact with the bottom electrode. The actuation of the micro-switch consists of an input voltage signal to the side electrodes that releases the pulled-in cantilever and opens the switch. As the input (side voltage) vanishes, the attractive force of the bottom electrode causes pull-in again. Pull-in can cause failure in the switches because of repeated use, but with the electrostatic levitation scheme, the switch can be better controlled and avoid destruction.

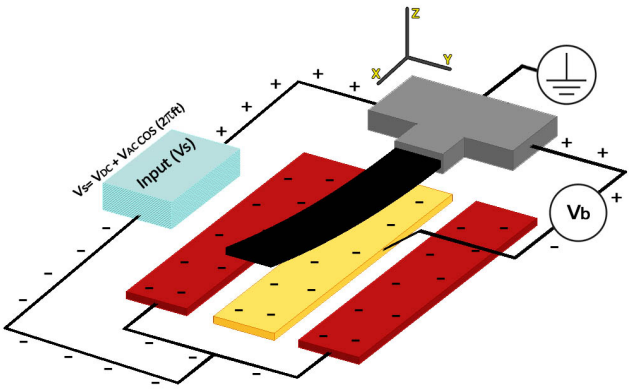

Fig. 4: Levitation-based micro-switch mechanism at OFF (open) state by charging the side electrodes with an input voltage signal. The strong fringe field overcomes the attraction force of the gap-closing electrodes in addition to the adhesion forces between the micro-switch cantilever tip and the contact area.

Parameter	Symbol	Value
Beam Length	L	505 μm
Beam Width	b_3	20.5 μm
Beam Thickness	h_3	2 μm
Module of Elasticity	E	160 GPa
Density	ρ	2330 kg/m^3
Initial Gap	d	2 μm
Bottom Electrode Width	b_2	32 μm
Side Electrode Width	b_1	28 μm
Electrode Thickness	h_1	0.5 μm
Dimple Height	h_d	0.75 μm

Table 1: Micro-switch properties and geometry

3 Mathematical Modeling

In this section, we present a model that describes the static and dynamic behaviors of a micro-switch in two electrostatic fields.
The switch of interest is a rectangular micro-beam with fixed-free boundary conditions. The effect of side and bottom electrodes are modeled as conservative forces. Moreover, the adhesion forces and the air pressure effect on dynamic and static characteristics of the switch are addressed in this model. We use x and t as the axial location and time. The x-axis passes through the centroid of the beam. The beam is considered as a continuous system and the transverse displacement is denoted by $\hat{w}(\hat{x},\hat{t})$ and $\hat{w}(\hat{x},\hat{t})+d$ represents the gap between the micro-beam and the substrate. According to the PolyMUMPS MEMS fabrication standard, the cross section area, the second moment of area about the x-axis, and the material distribution are uniform along the x-axis. Neglecting the out of plane deflection, We assume the strain energy is approximated by,

$$E_{strain} \approx EI\left(\frac{\partial^2 \hat{w}}{\partial x^2}\right)^2 \tag{1}$$

where E and I are the beam elastic modulus and the second moment of area about the x-axis. The equation of motion is then approximated by the Euler-Bernoulli beam theory.

$$\rho A\frac{\partial^2 \hat{w}}{\partial \hat{t}^2}+\hat{c}\frac{\partial \hat{w}}{\partial \hat{t}}+EI\frac{\partial^4 \hat{w}}{\partial \hat{x}^4}=\hat{f}_{sur}(\hat{w},\hat{t})+\hat{f}_e(\hat{w},\hat{x},\hat{t}) \tag{2}$$

where $A = b_3h_1$ and $\hat{f}_e(\hat{w},\hat{x},\hat{t})$ represent the beam cross-sectional area and the electrostatic forces, respectively. $\hat{f}_{sur}(\hat{w},\hat{t})$ denotes the adhesion force of the closed switch (pull-in position) between the micro-beam tip and its substrate.

Although Eq. (2) is not the most accurate beam model, since 1750 it has been a good enough method for many applications in large and small (micron) sizes. The model assumes the plane section of the beam remains plane after deformation according to thin beam theory. The shear and torsional stresses are assumed to be small. The shear forces are important for a short beam length while the switch is considered as a long beam. Introducing the nondimensioanl variables as listed in Table 2, one can get the nondimensional (ND) equation of motion:

$$\frac{\partial^2 w}{\partial t^2}+c\frac{\partial w}{\partial t}+\frac{\partial^4 w}{\partial x^4}=f_{sur}+f_e(w,x,t) \tag{3}$$

where

$$f_{sur}(w,t)=r\hat{f}_{sur} \tag{4}$$

$$f_e(w,t) = r\hat{f}_e(\hat{w}/h, \hat{x}/L, \hat{t}/T) \quad (5)$$

Using 2D simulations of the electric field in COMSOL, we have obtained capacitance terms for the potential energy function and the derivative of the potential energy with respect to the gap, which yields different force elements as described in [36]. The force term turns out to be made up of three elements. The levitation force, f_{11} and gap-closing force, f_{22} are related to the side electrodes and the bottom electrode respectively. The interaction between the existing electrostatic fields induces another force term f_{12} which depends on both side and bias voltages. Then, using the simulation data, we choose appropriate fitting functions for electrostatic force components f_{11}, f_{12} and f_{22} to the gap size. The levitation force ($f_{11}(w,t)$) and the interaction between electrostatic fields ($f_{12}(w,t)$) are approximated by 9'th order polynomial functions as

$$f_{11}(w) = \sum_{j=0}^{9} a_j w^j \quad (6)$$

$$f_{12}(w) = \sum_{j=0}^{9} b_j w^j \quad (7)$$

The gap-closing electrodes create an attractive force that diverges to infinity as the electrodes near each other but converges to zero if they get far enough apart. Using polynomial representation, this force must have been expanded to 20^{th} order polynomial function. Our best fitting function in a form of a fractional power function is apt for the gap-closing force that is influenced by the fringe field.

$$f_{22}(w) = \frac{\beta}{(w+1)^{2.15}} \quad (8)$$

The estimated ND force term is calculated by adding the three components as,

$$f_e(w) = V_s^2(t) f_{11}(w,t) + V_s(t) V_b f_{12}(w,t) + V_b^2 f_{22}(w) \quad (9)$$

As mentioned, the micro-switch is a continuous system with four boundary conditions. Therefore, the absolute transverse displacement can be modeled as a summation of distinct components named as modes. Each mode has a shape function (mode shape) with respect to the system boundary conditions. Because each component satisfies the equation of motion and the boundary conditions, they can be analyzed separately. Galerkin's method is a discretization method that simplifies the system's partial differential equation by approximating it as a set of ordinary differential equations as following.

Actual Value	ND Value
Axial position	$x = \frac{\hat{x}}{L}$
Beam gap (μm)	$w = \frac{\hat{w}}{d}$
Time	$t = \frac{\hat{t}}{T}$
Time constant	$T = \sqrt{\frac{\rho A L^4}{EI}}$
Damping coefficient	$c = \frac{\hat{c} L^4}{EIT}$
Force Constant	$r = \frac{L^4}{EIh}$

Table 2: Nondimentionalizaion of the system PDE

$$w(x,t) = \sum_{n=1}^{N} \phi_n(x) q_n(t) \quad (10)$$

where N is the number of the modes considered in the model, $\phi_n(x)$ and $q_n(t)$ are the n'th shape function and time function, respectively. Then, Eq. (10) is substituted into Eq. (3) to obtain the set of ODE's as,

$$\phi_n \frac{\partial^2 q_n}{\partial t^2} + c\phi_n \frac{\partial q_n}{\partial t} + \frac{\partial^4 \phi_n}{\partial x^4} q_n = f_{sur}(\phi_n q_n, t) + f_e(\phi_n q_n, x, t) \quad (11)$$

Considering the orthogonality of the mode shapes, Eq. (11) is multiplied by $\phi_n(x)$ and then integrated over the length of the beam.

$$\int_0^1 \phi_n^2 dx \frac{\partial^2 q_n}{\partial t^2} + c\int_0^1 \phi_n^2 dx \frac{\partial q_n}{\partial t} + \int_0^1 \frac{\partial^4 \phi_n}{\partial x^4} \phi_n dx q_n = \int_0^1 \phi_n f_{sur}(\phi_n q_n, t) dx + \int_0^1 \phi_n f_e(\phi_n q_n, x, t) dx \quad (12)$$

One shape function is used to discretize the system equation Eq. (3) as in Eq. (13).

$$m\frac{\partial^2 q}{\partial t^2} + cm\frac{\partial q}{\partial t} + kq = \int_0^1 \phi f_{sur}(\phi q, t) dx + \int_0^1 \phi f_e(\phi q, x, t) dx \quad (13)$$

where,

$$m = \int_0^1 \phi^2 dx \quad (14)$$

$$k = \int_0^1 \frac{\partial^4 \phi}{\partial x^4} \phi dx \quad (15)$$

As verified in [36], the Galerkin's reduced order method is used to obtain the discrete form of the nondimensional beam partial differential equation satisfying $\phi(0) = 0$, $\phi'(0) = 0$, $\phi''(1) = 0$, $\phi'''(1) = 0$:

$$\Phi(x) = cosh(\lambda x) - cos(\lambda x) + C(sinh(\lambda x) - sin(\lambda x)) \quad (16)$$

Considering the first cantilever mode shape, $C = 0.7341$ and $\lambda = 1.875$ in Eq. (16). Substituting Eq. (16) into the right side of Eq. (13) gives,

$$F_{11}(q,t) = V_s^2 \sum_{j=0}^{9} A_j q^j \quad (17)$$

$$F_{12}(q,t) = V_s V_b \sum_{j=0}^{9} B_j q^j \quad (18)$$

Moreover, according to the COMSOL results [36], the attractive force component can be represented as a function of q as following.

$$F_{22}(q) = V_b^2 \frac{\beta}{(q+1)^{2.15}} \quad (19)$$

When the micro-cantilever beam is close to the bottom electrode, the gap-closing force, F_{22}, is the dominant component. For the positions away from the substrate, the effect of the side electrodes, F_{11}, is greater compared to the other two forces. The electrostatic field decreases as the movable electrode goes further away from the bottom. The gap-closing electrostatic force (F_{22}) grows rapidly as the micro-cantilever gets close to the bottom electrode and as a consequence, the resultant force goes to infinity. More specifically, the effect of gap-closing force is more prominent between 0 to 4 μm. For high amplitude motions, the levitation force, F_{11} is the dominant driving force for the system. The electrostatic interaction force, F_{12}, influences in between and is at least one order of magnitude smaller than the other forces. The force coefficients of Eq. 17, 18, 19 are listed in Table. 3.

At this point, the continuous switch system and the force terms have been approximated by the first mode as in Eq. (20).

$$m\frac{\partial^2 q}{\partial t^2} + cm\frac{\partial q}{\partial t} + kq = F_{sur} + F_{11}(q,t) + F_{12}(q,t) + F_{22}(q) \quad (20)$$

Note that once the switch is released, the adhesion force term vanishes from Eq. (20). Energy analysis is an efficient way to dynamic analysis such as phase portrait and pull-in instability. According to the law of conservation of energy, if there is no nonconservative work during a motion, the total energy of the system remains unchanged. The total energy of the system is made up of kinetic energy i.e. the energy related to a body in motion, and potential energy which accounts for the position of the body in a conservative force field. Eq. (20) is multiplied by a small virtual displacement $d\widetilde{q}$ and then integrated over the range of motion.

$$\int_0^q (m\frac{\partial^2 \widetilde{q}}{\partial t^2} + k\widetilde{q} - F_{sur} - F_{11}(\widetilde{q},t) - F_{12}(\widetilde{q},t) - F_{22}(\widetilde{q}))d\widetilde{q} = E_t \quad (21)$$

Parameter	Value	Parameter	Value
A_0	1.84×10^{-3}	B_0	3.21×10^{-3}
A_1	1.38×10^{-4}	B_1	-2.91×10^{-3}
A_2	1.02×10^{-4}	B_2	9.74×10^{-4}
A_3	1.86×10^{-5}	B_3	-2.55×10^{-4}
A_4	-1.27×10^{-6}	B_4	5.43×10^{-5}
A_5	-1.38×10^{-7}	B_5	-8.52×10^{-6}
A_6	3.70×10^{-9}	B_6	8.97×10^{-7}
A_7	-3.29×10^{-9}	B_7	-5.88×10^{-8}
A_8	1.39×10^{-11}	B_8	2.13×10^{-9}
A_9	-2.31×10^{-12}	B_9	-3.33×10^{-11}
β	-0.463		

Table 3: The electrostatic force coefficients obtained from COMSOL simulations.

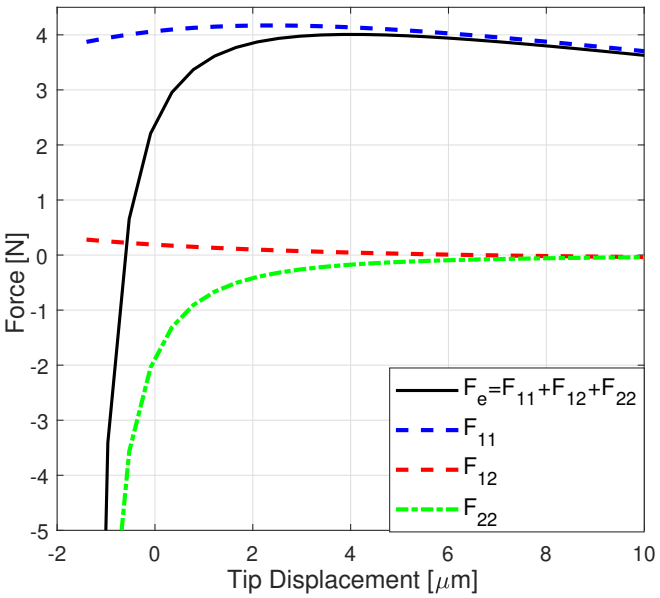

Fig. 5: Electrostatic force of a levitation-based microswitch and its components with $V_b = 2$ V and $V_s = 75$ V. The data has been obtained from the COMSOL simulation and using Eqs. (17,18,19). F_e: total force, F_{11}: repulsive force, F_{12}: interaction between electrostatic fields, F_{22}: gap-closing force.

Using Eq. (17),Eq. (18),Eq. (19), the $F_{11}(q,t)$, $F_{12}(q,t)$ and $F_{22}(q)$ are substituted in Eq. (21).

$$\frac{m}{2}(\frac{\partial q}{\partial t})^2 + \frac{k}{2}q^2 - \sum_{j=0}^{9}\frac{A_j}{j+1}q^{j+1} - \sum_{j=0}^{9}\frac{B_j}{j+1}q^{j+1} + \frac{\beta}{1.15(q+1)^{1.15}} = E_t \quad (22)$$

In Eq. (22), E_t is the total energy. We define the potential function $\pi(q)$ and the kinetic energy $T(\frac{\partial q}{\partial t})$ as

$$\pi(q) = \frac{k}{2}q^2 - \sum_{j=0}^{9}\frac{A_j}{j+1}q^{j+1} - \sum_{j=0}^{9}\frac{B_j}{j+1}q^{j+1} + \frac{\beta}{1.15(q+1)^{1.15}} \quad (23)$$

$$T(\frac{\partial q}{\partial t}) = \frac{m}{2}(\frac{\partial q}{\partial t})^2 \quad (24)$$

The energy equation Eq. (22) is re-written as,

$$T(\frac{\partial q}{\partial t}) + \pi(q) = E_t \quad (25)$$

As a result of Eq. (25), the nondimensionalized velocity $\frac{\partial q}{\partial t}$ is formulated as,

$$\frac{\partial q}{\partial t} = \pm\sqrt{\frac{2}{m}(E_t - \pi(q))} \quad (26)$$

Expanding Eq. (26) gives an explicit correlation between the ND displacement and ND velocity.

$$\frac{\partial q}{\partial t} = \pm[\frac{2}{m}(E_t - \frac{k}{2}q^2 + \sum_{j=0}^{9}\frac{A_j}{j+1}q^{j+1} + \sum_{j=0}^{9}\frac{B_j}{j+1}q^{j+1} - \frac{\beta}{1.15(q+1)^{1.15}})]^{\frac{1}{2}} \quad (27)$$

A phase portrait is an informative plot that indicates the system dynamics without engaging the time dimension in the analysis. Eq. (27) as a result of the energy equation Eq. (26) can predict the system trajectories as well as the dynamic pull-in instability.

4 Experimental Setup

The experimental setup to test the MEMS switch is shown in Fig.6. The micro-cantilever with the special electrode design (Figs. 3,4) was fabricated using PolyMUMPs standard fabrication performed by MEMSCAP

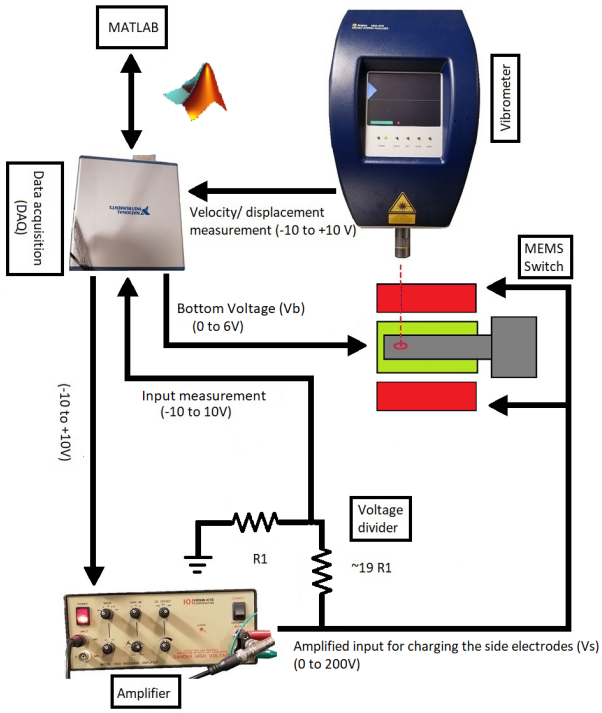

Fig. 6: Experimental setup.

[37]. An optical profiler was used to measure the dimensions including a sight tip curvature. The material properties and the design geometry can be found in Table. 1.

All the experiments were conducted at atmospheric pressure, at the lab temperature $22°C$, and with the relative humidity of 37 percent. The micro-beam tip displacement and velocity are measured with a laser vibrometer (Polytec MSA-500). The measured data are received and conveyed to MATLAB through a data acquisition system (National Instruments USB 6366 DAQ). The side voltage is provided by a wide-band amplifier (Krohn-Hite 7600). A DC power supply (B&K Precision 9110) supplies the bottom voltage. The side voltage is approximately 10 orders of magnitude greater than the bias voltage. The disparity is caused by the different electrostatic fields, i.e. attraction and levitation at the bottom and the side electrodes, respectively. The voltages are manipulated with MATLAB and the outputs are measured by two electrometers (Keithley 6514) and transferred to MATLAB again through the data acquisition system.

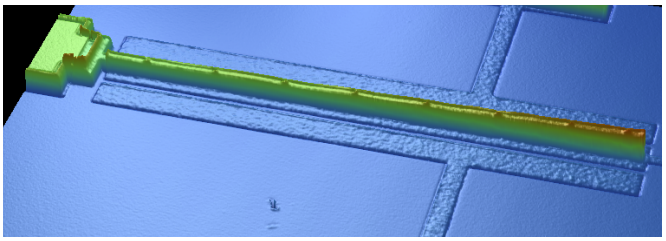

Fig. 7: Optical image of the micro-switch cantilever. The beam tip is initially curved upward because of residual stresses during fabrication.

5 Static Characterization

The static behavior of the micro-switch is analyzed in this section. The importance of static analysis is the identification of the stiffness and mechanism nonlinearities. It helps to understand about the electrostatic force data of the side and bottom electrodes obtained from COMSOL. The system behavior for a static actuation (i.e. by the DC side voltage and DC bottom voltage) is important information about micro-switches. Secondly, as mentioned in the mechanism description section, the presented switch is normally closed as the micro-beam is initially in the pull-in position. Therefore, studying the static pull-in is crucial for designing dimensions as well as electrical design parameters. In this case, electrostatic and adhesion forces influence the stiction of the micro-beam which will be discussed explicitly.

The effect of the initial curl of the micro-beam was not negligible and was considered in the analysis. Using the optical imaging (See Fig. 7), the cantilever beam tip curvature is between 0.5 and 2 μm. The initial beam gap is 2 μm between the cantilever base and the substrate. Dimples restrict the downward motion range to 1.25 μm. Therefore, the order of magnitude of the initial curl in comparison with the initial gap is not negligible and should be considered in calculations. For this purpose, an average curl of 1.5 μm is added to the tip displacement.

5.1 Static pull-in and static displacement

For designing MEMS devices, static pull-in refers to the system instability that occurs when the restoring force of the movable electrode cannot overcome the electrostatic force. In this situation, the movable electrode collapses and collides with the bottom electrode. Restricted operational range and possible permanent stiction are the consequences of pull-in instability. In many MEMS devices, pull-in is an undesirable feature, but it is the main operating mechanism for micro-switches.

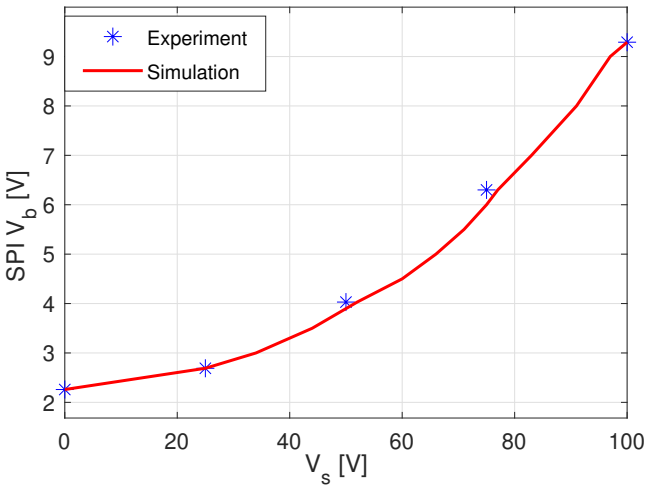

Fig. 8: Static pull-in bottom voltage $V_{b,SPI}$ in the presence of different side voltages V_s as the micro-switch closes. the bottom voltage is increased slowly in a way that the least motion is observed. Both axes represent the data in volts.

In the present work, the switch of interest is an initially pulled-in, or closed, switch. In the following, we will demonstrate how the static pull-in happens in a levitation-based micro-switch. Consider an open switch in which a 50 V input signal ($V_s = 50\ V$) is applied to the side voltage. Then, the bottom voltage is increased very slowly in a way that no oscillation takes place. At each increment of the bottom voltage, the micro-cantilever tip bends downward and stands at the stable equilibrium point corresponding to the side and bottom voltage. This process is continued until reaching the static pull-in bottom voltage $V_{b,SPI}$ where the system loses stability and accelerates toward the bottom electrode.
Eq. (20) in static analysis is simplified as,

$$kq = F_{11}(q) + F_{12}(q) + F_{22}(q) \tag{28}$$

F_{11}, F_{12}, and F_{22} are the electrostatic force terms used in Eq. (17), Eq. (18), Eq. (19) and are described in the mathematical modeling section. Eq. (28), is a nonlinear algebraic equation that is solved using numerical methods of root finding. For a constant side voltage, at $V_{b,SPI}$ this equation does not have any real root. Our goal is to find the $V_{b,SPI}$ corresponding to different side voltages. The static pull-in bottom voltage in the presence of different input voltage amplitudes (V_s) is reported as in Fig. 8.

At a constant side voltage for $V_b < V_{b,SPI}$, the solution of Eq. (28) gives two distinct equilibrium points. To evaluate the calculated fixed-points, the eigen-values of the system Jacobian matrix J are determined. The

system Eq. (20), is represented in the state space as,

$$\left\{\begin{array}{c} \dot{u}_1 = u_2 \\ \dot{u}_2 = -ku_1 - cu_2 + F_{11}(u_1,t) + F_{12}(u_1,t) + F_{22}(u_1) \end{array}\right\} \tag{29}$$

where u_1, u_2 are the system states representing nondimensional tip displacement and velocity, and $\dot{u}_1$, $\dot{u}_2$ are their time derivatives. Fixed-points of the system are the equilibrium positions and are calculated by equating the right-hand side of the state space to zero. As a result, $u_{2e} = 0$, and u_{1e} is the same as the solution of Eq. (28). After dropping the damping effect, the Jacobian matrix is defined as,

$$J(V_b, V_s, u_1) = \begin{bmatrix} 0 & 1 \\ -k + \frac{\partial F_{11}}{\partial u_1} + \frac{\partial F_{12}}{\partial u_1} + \frac{\partial F_{22}}{\partial u_1} & 0 \end{bmatrix} \tag{30}$$

Substituting the fixed-points (u_{1e}) obtained from Eq. (29), and the corresponding side and bottom voltages, and neglecting the damping effect in the static analysis, the eigen-values (λ) of the Jacobian matrix are calculated. The equilibrium point u_{1e} is stable if its eigenvalue set includes non-positive real parts in which the fixed-point is called the center. Calculating the eigenvalues of Eq. (30) reveals that for each pair of side V_s and bottom voltage $V_b < V_{b,SPI}$, the system will have one stable (q_s) and one unstable equilibrium point (q_u). Beyond the static pull-in bottom voltage i.e. $V_b > V_{b,SPI}$ Eq. (28) has no real solution. Hence, there will be no equilibrium and the system diverges and sticks to the substrate. Fig. 8 shows the static pull-in results obtained from the eigenvalue analysis of Eq. (30).
To demonstrate the bifurcated behavior of the switch, we illustrate the static displacement of the switch as a function of side voltage for various bottom voltages, see Fig. 9. As seen in Figs. (9a, 9b), $V_b = 2\,V$ is not enough to close the switch because at $V_s = 0\,V$ the system has a stable fixed-point. As seen in Fig. 8, the minimum bottom voltage for static pull-in is $V_{b,SPI} = 2.26\,V$. Figs. (9c, 9d) show that $V_s = 79\,V$ and $49\,V$ are the saddle-node bifurcation points of the system equilibrium Eq. (31) in the presence of DC bottom voltages $V_b = 2\,V$ and $4\,V$ respectively, where the stable and unstable branches meet and end.

The side voltage can act as a knob to tune the behavior of the MEMS switch. This effect is demonstrated by taking a constant bottom voltage and varying the side voltage. For each V_b, there is a threshold side voltage beyond which the Eq. (28) has no real root. The simulation results are demonstrated in Fig. 10. One can deduce that the side voltage increases the pull-in voltage of the MEMS switch.

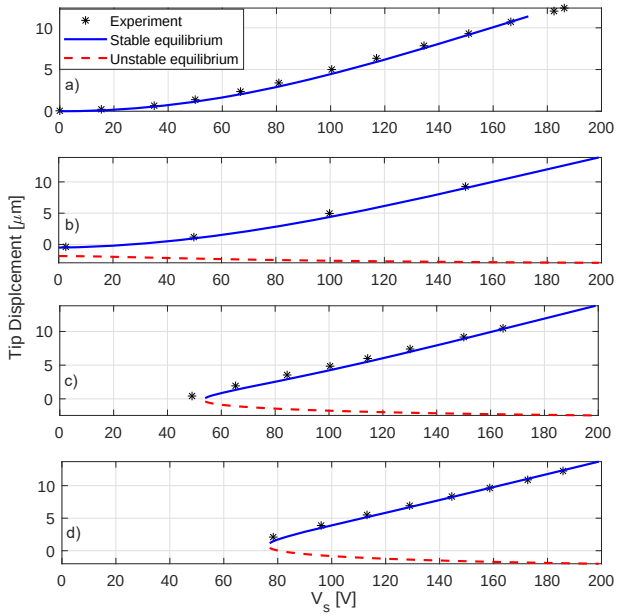

Fig. 9: Static displacement of the micro-switch tip versus side voltage in the presence of $V_b = 0V$ (a), $V_b = 2V$ (b), $V_b = 4\,V$ (c) and $V_b = 6\,V$ (d).

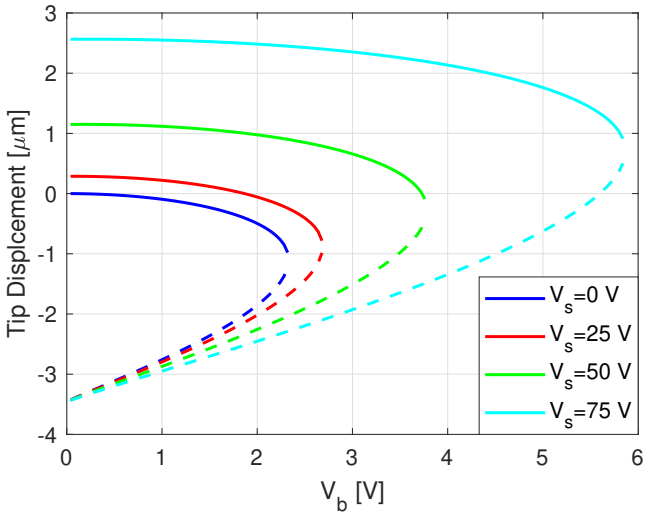

Fig. 10: Simulation results for micro-switch tip displacement in the presence of constant side voltages. The solid and dashed lines represent the stable and unstable equilibrium points. The cross marks indicate the minimum bottom voltage for initiating the switch closing process at the saddle-node bifurcation.

5.2 Release (opening process)

In the pull-in position, an adhesion force is added to the electrostatic and spring forces. This fact is observed when the required levitation force for opening the micro-switch is more than the expected amount. Because of dimples, the maximum distance the micro-beam tip can drop is 1.25 μm instead of the $d = 2\mu m$ for a completely flat movable electrode. In this case, the static equation will be,

$$kq = F_{11}(q) + F_{12}(q) + F_{22}(q) + F_{sur} \tag{31}$$

where $F_{sur}(q)$ is the surface force between the micro-beam dimples and the substrate. Because the model was validated by static displacement, static pull-in and dynamic pull-in (which will be discussed later), we can evaluate the adhesion force on a pulled-in micro-beam. As seen in Fig. 8, the minimum bottom voltage for initiating static pull-in is 2.26 V, which happens when $V_s = 0\,V$. We expected that a bottom voltage less than 2.26 V cannot hold the beam in pull-in position. While the experiments show that when the bottom voltage is reduced to less than $V_b = 1.3\,V$, the micro-beam was kept closed. Below this threshold, the spring force could overcome the attraction force and the micro-beam was released from the pull-in. This test implies that when the only electrostatic force is the attraction of the bottom electrode, a pulled-in micro-beam keeps sticking if $V_b > 1.3\,V$. The mentioned test also verifies the existence of an extra force during the release instant i.e. the surface force F_{sur} between the two layers. While the open switch is governed by Eq. (28), the balance of forces at the pulled-in system is obtained as

$$k(-1 + h_d/d) = F_{11}(-1+h_d/d)+F_{12}(-1+h_d/d)+F_{22}(-1+h_d/d)+F_{sur} \tag{32}$$

Using this equation, the surface force can be expressed as

$$F_{sur} = -V_s^2 \sum_{j=0}^{9} A_j(-1+h_d/d)^j - V_s V_b \sum_{j=0}^{9} B_j(-1+h_d/d)^j - V_b^2 \frac{\beta}{(h_d/d)^{2.15}} + k(-1 + h_d/d) \tag{33}$$

Assume a micro-cantilever is pulled-in with the bias voltage, V_b. Dropping the surface force yields

$$0 = \alpha_0 + \alpha_{11} V_{s,0}^2 + \alpha_{12} V_{s,0} V_b + \alpha_{22} V_b^2 \tag{34}$$

where $\alpha_0 = k(-1 + h_d/d)$, $\alpha_{11} = -\sum_{j=0}^{9} A_j(-1 + h_d/d)^j$, $\alpha_{12} = -\sum_{j=0}^{9} B_j(-1+h_d/d)^j$, $\alpha_{22} = -\frac{\beta}{(h_d/d)^{2.15}}$.

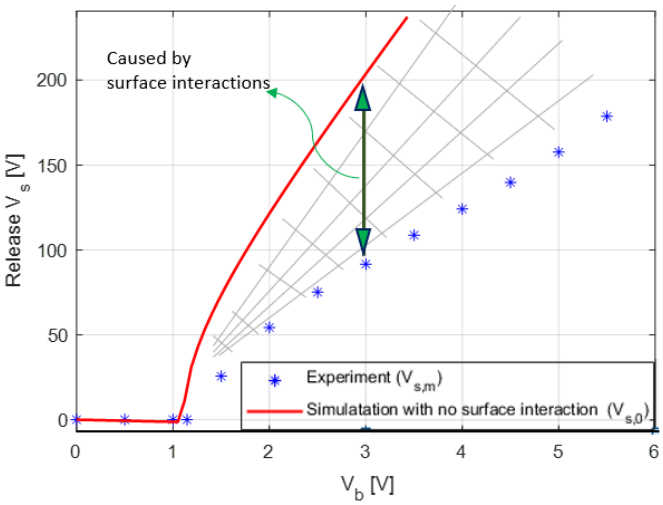

Fig. 11: Release side voltage (V_{rs}) required for opening a closed micro-switch as the the bottom voltage of V_b varies. The meshed area demonstrates the difference between the simulation results assuming no surface interaction and the experimental results.

The release side voltage corresponding to zero surface force is called $V_{s,0}$ and can be obtained by solving Eq. (34) as

$$V_{s,0} = \frac{1}{2\alpha_{11}}(-\alpha_{12} V_b + \sqrt{\alpha_{12}^2 V_b^2 - 4\alpha_{11}(\alpha_0 + \alpha_{22} V_b^2)}) \tag{35}$$

The results of theoretical side voltage assuming zero surface force are plotted against measurements in Fig. 11. The testing conditions are 1 atm, 22°C, 37 percent relative humidity. As shown, the theoretical method of Eq. (34) can successfully predict the minimum bottom voltage required for keeping the beam at the pull-in position ($V_b \approx 1.2$ V). However, for larger values of V_b the required release side voltage is significantly smaller the calculated value when the surface force is neglected. It implies that the surface force resists the stiction during the pull-in position and is repulsive.
By subtracting Eq. (34) from Eq. (33), one obtains an expression for F_{sur} as a function of the theoretical side voltage (corresponding to zero surface force), $V_{s,0}$, and the measured side voltage $V_{s,m}$ as

$$F_{sur} = \alpha_{11}(V_{s,m}^2 - V_{s,0}^2) + \alpha_{12}(V_{s,m} - V_{s,0}) \tag{36}$$

As shown in Fig. 5, the effect of α_{12} is insignificant in comparison with α_{11} and α_{22}. Hence, Eq. (36) is approximated by

$$F_{sur} \approx \alpha_{11}(V_{s,m}^2 - V_{s,0}^2) \tag{37}$$

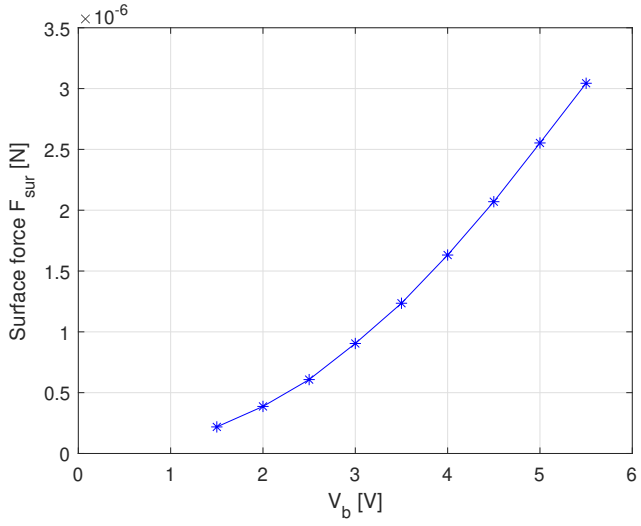

Fig. 12: Surface force in the release instant in the presence of different bottom voltages. The positive direction of the vertical axis means the surface forces are repulsive at the release instant.

Using Eq. (37), the surface force is plotted in Fig. 12. The surface force is found to be repulsive and not adhesive at the release instant. The nature of repulsive surface force can explain why the measured side voltage is lower than the theoretical voltage that does not consider the effect of surface force (Fig. 11).

6 Dynamic Characterization

In this section, we will investigate the micro-switch characteristics considering dynamic pull-in, time response, frequency response, and basins of attraction. A thorough design requires a close look at the switch dynamics as the switch experiences dynamical motion during opening and closing. In this section, the relationship between the motion of the movable electrode and side/bottom voltages as well as the switch operation in the presence of AC inputs is studied.

6.1 Dynamic pull-in (closing process)

This section considers the dynamic pull-in in the presence of DC side and bottom voltages and explains the difference between static and dynamic pull-in. The static pull-in refers to saddle-node bifurcation points, where stable and unstable equilibrium points meet and there is no equilibrium point beyond that. This definition does not include the effect of any kind of motion. The switch is in continuous motion. As a result, the switch's movable electrode accelerates and gains kinetic energy. In this case, the stability analysis depends on kinetic energy. The initial conditions can cause dynamic pull-in instability. For closing process, a DC voltage is applied to the bottom electrode. The micro-beam accelerates toward the bottom electrode and if the voltage is sufficiently large, the system, loses stability and dynamic pull-in happens. We use an energy approach to model the dynamic pull-in. Consider an open micro-switch depicted in Fig. 4, where the micro-beam is levitated at the height of q_0 by applying V_s to the side electrode. At this time, V_b is given to the bottom electrode causing the beam tip to move downward. Using Eq. (23) and Eq. (24), the initial potential and kinetic energy will be,

$$\pi_0 = \pi(q_s) \tag{38}$$

$$T_0 = T(0) = 0 \tag{39}$$

As in Eq. (25), the total energy is the summation of kinetic and potential energy, where in this case it will be,

$$E_t = T_0 + \pi_0 = \pi(q_s) \tag{40}$$

Dynamic pull-in happens when the system fails to find a stable oscillation around a stable equilibrium point. In this situation, the system will be non-oscillatory, it loses stability and collapses to the bottom electrode.

The demonstration of the potential and total energy of the system provides an interesting perspective of the system pull-in dynamics. Fig. 13 shows potential functions plotted using Eq. (23) for different bottom voltages with a constant side voltage $V_s = 50\,V$. For $V_b < 3.3V$, the beam starts moving from $2.8\,\mu m$ and oscillates around the static equilibrium point corresponding to $V_s = 50\,V$. Initially at $q(0) = q_s$ (i.e. the static equilibrium point corresponding to $V_s = 50\,V, V_b = 0\,V$), we apply the DC bottom voltage. Fig. 14 depicts the phase portrait for different bottom voltages. Below the threshold of $V_b = 3.3\,V$, the micro-beam oscillates around a center. For $V_b = V_{b,DPI}$ and beyond this threshold, the system begins dynamic pull-in instability. This voltage is called dynamic pull-in bottom voltage $V_{b,DPI}$ corresponding to a constant side voltage. The bottom dynamic pull-in voltage is about $V_b = 2.05V$ for $Vs = 0V$. It is noted that the bottom dynamic pull-in voltage is about $V_b = 3.3\,V$ for $V_s = 50\,V$, while the static pull-in for the side voltage of $Vs = 50\,V$ occurs at $V_b = 3.9\,V$ (Figs. 8,15).

The identification of this dynamic pull-in point is a considerable parameter in the design of MEMS switches [38]. Dynamic pull-in voltages from simulations and experiments are compared in Fig. 15. For each data point,

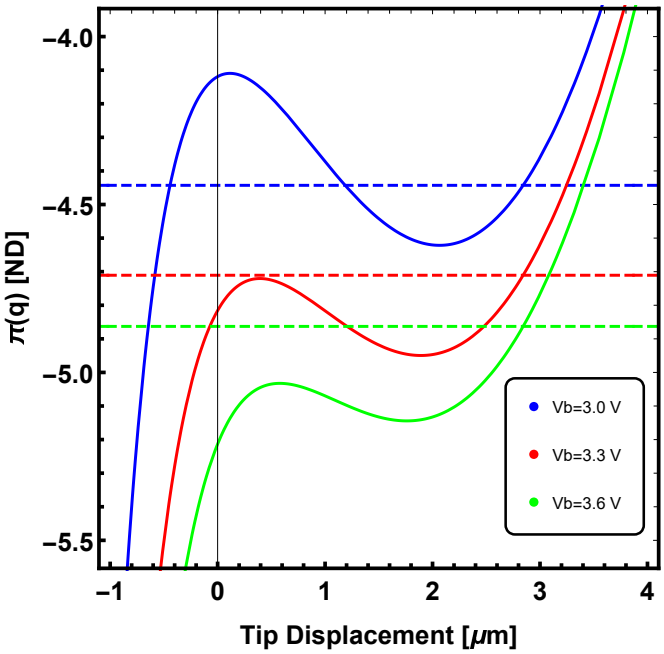

Fig. 13: Potential energy as a function of tip displacement for various bottom voltages. The dashed line represents the initial level of energy of the system for Vs=50 V. The dashed lines show the total energy level of each test.

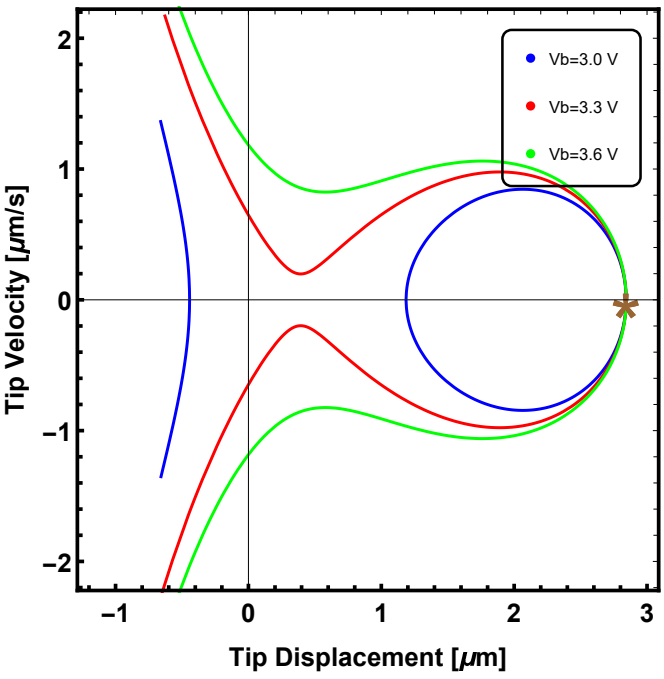

Fig. 14: Phase-portrait of the micro-switch with a constant side voltage $V_s = 50\,V$. The brown mark shows the initial condition of the switch levitation as a result of the side voltage.

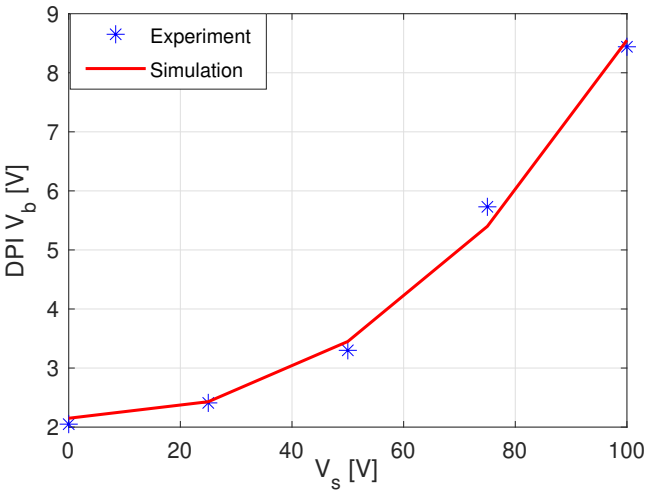

Fig. 15: Dynamic pull-in bottom voltage $V_{b,DPI}$ in the presence of different side voltages V_s in the closing process of the micro-switch. For each data point, the micro-beam is initially in the stable equilibrium point corresponding to the side voltage without bottom voltage. A sudden bottom voltage that causes the collapse is then recorded.

the micro-beam is initially in the stable equilibrium point corresponding to the side voltage without bottom voltage. Then, a sudden bottom voltage is applied and the value that causes dynamic pull-in is recorded in this graph. This result shows that the levitation force is raised as the side voltage is increased. As a result, more attractive force is required to initiate dynamic pull-in instability. A stronger levitation force also results in a greater upward displacement and it is another reason for requiring more attractive force. Such a characteristic can be considered as a tuning parameter for the triggering-threshold of micro-devices. As explained in the mechanism description section, the triggering signal for opening the micro-switch is a DC voltage (V_s) signal that is transferred to the side electrodes.

6.2 Time response

The time solution of the system is approximated by Galerkin's reduced order method. The nondimensional Eq. (20) gives an estimation of the micro-beam tip motion. The ODE45 solver of MATLAB with a tolerance of 10^{-6} is used for this purpose. The switch time response after release in the presence of a DC bottom voltage of $V_b = 2.5\,V$, delivers useful information regarding the dynamic characterization of the micro-switch. Fig. 16 shows the switch release during the opening process. Pulses with different amplitudes were applied as the

input side voltage signal. The solution of Eq. (20) estimates 5% relative error for $V_s = 100\,V$ and about 10% error for $V_s = 120\,V$. The damping coefficient plays an important role during the transient response, while it does not affect the steady-state response of a switch actuated by DC side and bottom voltages. We tried to choose a value that predicts the dynamics in the best way. The damping nondimensional coefficient was identified to be $c = 0.00733$ from comparing the simulation with experimental results.

To obtain a better understanding of the two-way operation of the switch, we demonstrate the switch opening and closing process, see Fig. 17. First, the bottom electrode is fed a ramp function from 0 to 4.5 Volt and then it is reduced to $V_b = 2.5\,V$ and remains at that value. The open switch accelerates toward the substrate and DPI happens putting the switch in the ON position (star). At $t = 1.15\,sec$ (diamond) a voltage signal (V_s) with the pulse-width of 1 *sec* is applied to the side electrodes. The generated repulsive force detaches the pulled-in cantilever and the switch goes to the OFF position (triangle pointing upward). A closer look at the opening process can be found in Fig. 16 The released micro-cantilever is held at 4 and 6 μm (2x and 3x the initial gap) for the input magnitudes $V_s = 100\,V$ and $120\,V$, respectively. Our simulations can closely capture the measured response of the switch and can be used as a design tool for the optimization of switch behavior.

The switch closes when the side voltage is disconnected. Figure 17 shows when the input is disconnected at $t = 2.15\,sec$, the switch goes back to the ON position (triangle pointing downward). One can recognize a delay in the closing process after the disconnection of side voltage of 120 V. It originates from the high velocity the micro-switch tip gains as it approaches to the substrate. Air is compressed under the movable electrode and squeeze-film damping happens. As a result, a strong damping force will dissipate the switch's kinetic energy. The mentioned delay is not observed when the input amplitude is $V_s = 100\,V$. If the switch closing speed is essential for the user, it must be noted that the disconnection of large inputs ($V_s > 110\,V$) causes a significant delay when the switch is operating at $1\,atm$. The switch operation at lower pressure values will be much faster.

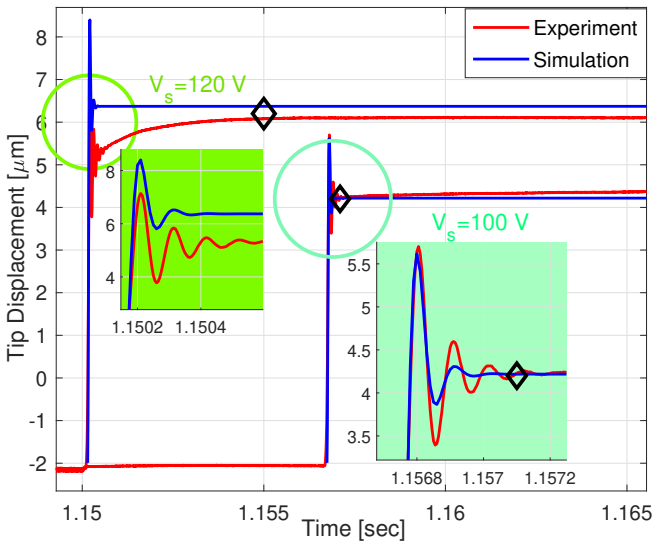

Fig. 16: Simulation and experimental time history of the micro-switch during the opening process with $V_s = 100\,V$, $120\,V$. The bottom voltage is $V_b = 2.5\,V$ at both tests.

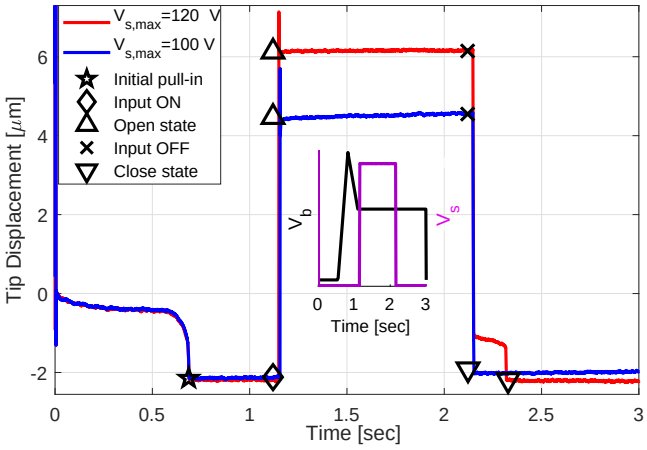

Fig. 17: Experimental time history of the micro-switch opening and closing processes recorded by Laser Vibrometer Polytec MSA-500. The bottom voltage $V_b = 2.5\,V$ is applied at $t = 0\,s$. Input voltages $V_s = 100\,V$ and $V_s = 120\,V$ are connected between $t = 1.15\,s$ and $t = 2.15\,s$.

6.3 Frequency responses and basins of attraction

The levitation-based switch mechanism enables large oscillations over a broader frequency range as the auxiliary actuation is applied in the opposite direction of the substrate (Fig. 4). Hence, the motion is not restricted and high amplitude motion is achievable for a broader frequency range, which is desirable for oscillators used in clock circuits. Considering the prototype we are using for experiments, a $505\,\mu m$ micro-cantilever with $2\,\mu m$ initial gap, the switch tip reaches $30\,\mu m$ as $V_s = 170\,V$ is given to the side electrodes. This is 15 times larger than the conventional gap-closing configuration. The mentioned attribute enables the mechanism with a potential to be used in optical switches. To

further validate our dynamic analysis, the frequency response is compared with the experimental results. The experiments are conducted at reduced pressure of 300 mTorr using a vacuum chamber. The low pressure environment enables observing the effect of nonlinearity on the increase of bandwidth of the combined mechanism.

The solution of the reduced-order dynamics Eq. (20) gives the nondimensional time solution in the presence of an electrostatic actuation. An alternating voltage is added to the side electrodes as a result of which the side voltage can be represented as,

$$V_s = V_{DC} + V_{AC}cos(2\pi ft) \tag{41}$$

where V_{DC} and V_{AC} stand for the DC and AC components of the side voltage, and f is the frequency of the alternating signal. Fig. 18 shows the amplitude frequency diagram in the presence of constant bottom voltages $V_b = 0\ V, 2\ V, 6\ V$. As in Fig. 18, the oscillation amplitude against the driving frequency is plotted. Considering the force approximation functions Eqs. (6-8), the side electrodes generate an electrostatic field because of which the system involves nonlinear terms. The dominant higher order components such as the quadratic and negative cubic terms of Eqs. (6,7) result in softening effect as the frequency response tilts left. Backward and forward sweeping was conducted to capture upper and lower branches. Comparing the two branches, the upper one consists of a higher energy level, while the lower branch addresses a low amplitude oscillation with a lower energy level at the same frequency. As seen in this figure, the higher bottom voltage allows the switch to maintain longer on the upper branch. As expected [12,36,39–41], the higher bottom voltage shifts the linear natural frequency to the left.

The initial conditions of the system determine the amplitude of the steady-state oscillations. To obtain an understanding of the region of the phase plane that leads to high or low oscillation orbits, the basins of attraction for the trajectories in the hysteresis region are obtained. For parallel-plate resonators, basins of attractions were introduced as a method to study the safety and reliability of the resonators against disturbances and mechanical shocks [42]. In this study, the simulations were conducted by long-time integration at three fixed frequency values selected from Fig. 18 (c) for the bias voltage of 6 V. 800 cycles were used to allow oscillations to reach the steady-state response. The maximum amplitude corresponding the last cycle was recorded. Simulations used 100 x 100 grid points for the initial conditions in the phase plane. The steady-state amplitude corresponding to the high amplitude branch was shown by a white dot and the low branch was depicted by a black dot, see Fig. 19. To avoid singularity arising

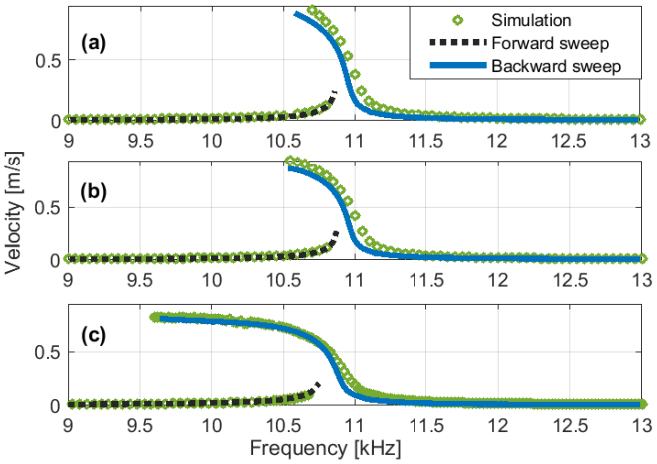

Fig. 18: Simulation and experiments of the micro-switch frequency response in the presence of the bottom voltage of $V_b = 0\ V$ (a), $V_b = 2\ V$ (b) and $V_b = 6\ V$ (c), and the side voltage of $V_s(t) = 170\ V + 0.5cos(2\pi ft)$. The backward (green) and forward (black) frequency sweep result in oscillation on upper and lower branch, respectively.

from the term F_{22} at dynamic pull-in, the denominator was allowed to go close but not reach zero. As the frequency reproaches the peak, the probability of landing on the high oscillation branch decreases because the basin of attraction for the higher branch shrinks. The basin of attraction gives an insight into the nonlinear behavior of the system that results from the combined electrode configuration.

7 Conclusion

The static and dynamic characteristics of a levitation-based micro-switch is presented in this paper. The mechanism consists of a well-known gap-closing micro-capacitor configuration with the addition of two fixed side electrodes that generate an upward force to the movable electrode. The movable electrode is a micro-beam fixed at one end and free at the other end. The proposed mechanism provides a controlled way of operating switches that has not been possible. If the side voltage is large enough, the switch is actuated and opens. The threshold side voltage for opening the switch is simply tuned by the bottom voltage. For example, $2\ V$ of bottom voltage requires at least $50\ V$ of side voltage to release. The micro-switch is then closed upon the disconnection of the side voltage. Experiments including static displacement, static pull-in, dynamic pull-in, release from pull-in position, frequency response, and the time history were conducted. A mathematical model is

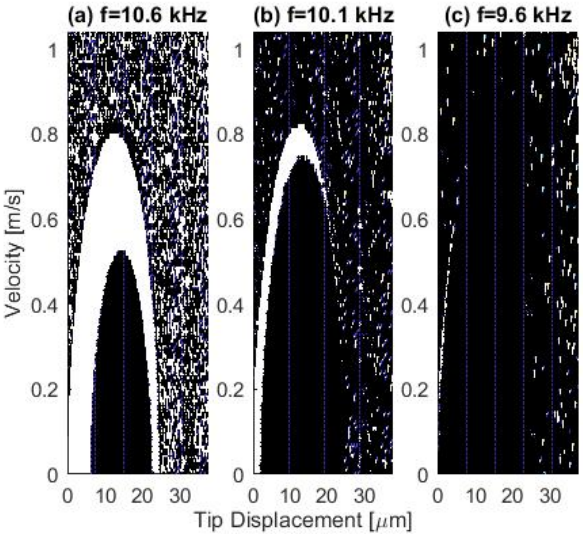

Fig. 19: Simulation results indicating the basins of attraction of the micro-switch nonlinear dynamics in the presence of the bottom voltage of $V_b = 6\ V$ and the side voltage of $V_s = 170\ V + 0.5cos(2\pi ft)$. The initial conditions are mapped to the steady state motions landing on the high oscillation branch (white color) and the low oscillation branch (black color) at three different frequencies in the hysteresis region. The intensity of the white points indicates greater probability.

presented and validated by experiments to delineate the fundamental operation of a normally closed and open switch. The simulation results capture the experimental results with good accuracy. The mathematical model can be used as a computationally efficient tool to design high-performance RF switches. Understanding the release features enables the designer to set an actuation threshold and tune the switch sensitivity.
To realize a wider practical outlook, the proposed idea can be further studied in various operating conditions with different humidity and temperature for harsh environment applications.

Acknowledgment

The authors would like to acknowledge the financial support of this study by the National Science Foundation (NSF) through grant CMMI 1919608.

Compliance with ethical standards

Conflict of interest The authors declare that they have no conflict of interest.

References

1. A Basu, GG Adams, and NE McGruer. A review of micro-contact physics, materials, and failure mechanisms in direct-contact rf mems switches. *Journal of Micromechanics and Microengineering*, 26(10):104004, 2016.
2. Pushpapraj Singh Sushil Kumar, Dhairya Singh Arya. Volatile or non-volatile switching? establishing design parameters for metal-contact relays using on/off hysteretic behavior (rt to 300°c). *Applied Physics Letters*, 2020.
3. RP Hennessy, A Basu, GG Adams, and NE McGruer. Hot-switched lifetime and damage characteristics of mems switch contacts. *Journal of Micromechanics and Microengineering*, 23(5):055003, 2013.
4. Mohammad R Vazirisereshk, Saima A Sumaiya, Ashlie Martini, and Mehmet Z Baykara. Measurement of electrical contact resistance at nanoscale gold-graphite interfaces. *Applied Physics Letters*, 115(9):091602, 2019.
5. Zhiqiang Chen, Wenchao Tian, and Xiaotong Zhang. Effect of surface asperities on the capacitances of capacitive rf mems switches. *Journal of Micromechanics and Microengineering*, 27(3):034002, 2017.
6. Hassen M Ouakad. Static response and natural frequencies of microbeams actuated by out-of-plane electrostatic fringing-fields. *International Journal of Non-Linear Mechanics*, 63:39–48, 2014.
7. Hassen M Ouakad. Electrostatic fringing-fields effects on the structural behavior of mems shallow arches. *Microsystem Technologies*, 24(3):1391–1399, 2018.
8. Yoav Linzon, Bojan Ilic, Stella Lulinsky, and Slava Krylov. Efficient parametric excitation of silicon-on-insulator microcantilever beams by fringing electrostatic fields. *Journal of Applied Physics*, 113(16):163508, 2013.
9. Slava Krylov, Bojan R Ilic, and Stella Lulinsky. Bistability of curved microbeams actuated by fringing electrostatic fields. *Nonlinear Dynamics*, 66(3):403–426, 2011.
10. Mohammad Tausiff, Hassen M Ouakad, Hussain Alqahtani, and Abdurahman Alofi. Local nonlinear dynamics of mems arches actuated by fringing-field electrostatic actuation. *Nonlinear Dynamics*, 95(4):2907–2921, 2019.
11. Prashant N Kambali and Ashok Kumar Pandey. Nonlinear response of a microbeam under combined direct and fringing field excitation. *Journal of Computational and Nonlinear Dynamics*, 10(5), 2015.
12. M. Pallay, M. Daeichin, and S. Towfighian. Dynamic behavior of an electrostatic mems resonator with repulsive actuation. *Nonlinear Dynamics*, 89(2), 2017.
13. M. Pallay and S. Towfighian. A reliable mems switch using electrostatic levitation. *Applied Physics Letter*, 2018.
14. Shahrzad Towfighian, Abdulrahman Seleim, Eihab Abdel-Rahman, and Glenn Heppler. A large-stroke electrostatic micro-actuator. *Journal of Micromechanics and Microengineering*, 21(7), 2011.
15. M. Daeichin, M. Ozdogan, S. Towfighian, and R. N. Miles. Dynamic response of a tunable mems accelerometer based on repulsive force. *Sensors & Actuators: A. Physical*, 2019.
16. Mehmet Ozdogan, Shahrzad Towfighian, and Ronald Miles. A mems microphone with repulsive sensing. *The Journal of the Acoustical Society of America*, 141(5), 2017.
17. Meysam Daeichin, Ronald Miles, and Shahrzad Towfighian. Lateral pull-in instability of electrostatic mems transducers employing repulsive force. *NONLINEAR DYNAMICS*, 2020.
18. Mehmet Ozdogan, Shahrzad Towfighian, and Ronald N Miles. Modeling and characterization of a pull-in free

mems microphone. *IEEE Sensors Journal*, 20(12):6314–6323, 2020.
19. Mark Pallay, Ronald N Miles, and Shahrzad Towfighian. Towards a high bias voltage mems filter using electrostatic levitation. *Mechanical Systems and Signal Processing*, 150:107250, 2020.
20. Brian McCarthy, George G Adams, Nicol E McGruer, and David Potter. A dynamic model, including contact bounce, of an electrostatically actuated microswitch. *Journal of microelectromechanical systems*, 11(3):276–283, 2002.
21. Andrea Guerrieri, Attilio Frangi, and Luca Falorni. An investigation on the effects of contact in mems oscillators. *Journal of Microelectromechanical Systems*, 27(6):963–972, 2018.
22. K Girija Sravani and K Srinivasa Rao. Analysis of rf mems shunt capacitive switch with uniform and non-uniform meanders. *Microsystem Technologies*, 24(2):1309–1315, 2018.
23. Jae-Ik Lee, Youngsup Song, Hakkyun Jung, Jungwook Choi, Youngkee Eun, and Jongbaeg Kim. Deformable carbon nanotube-contact pads for inertial microswitch to extend contact time. *IEEE Transactions on Industrial Electronics*, 59(12):4914–4920, 2011.
24. Wenchao Tian and Zhiqiang Chen. Analysis of bistable inductive micro-switch based on surface micro size effect. *Applied Surface Science*, 334:32–39, 2015.
25. John-Ojur Dennis, Abdelaziz-Yousif Ahmed, and Mohd-Haris Khir. Fabrication and characterization of a cmos-mems humidity sensor. *Sensors*, 15(7):16674–16687, 2015.
26. Bharat Bhushan. Adhesion and stiction: mechanisms, measurement techniques, and methods for reduction. *Journal of Vacuum Science & Technology B: Microelectronics and Nanometer Structures Processing, Measurement, and Phenomena*, 21(6):2262–2296, 2003.
27. Bharat Bhushan, Yong Chae Jung, and Kerstin Koch. Micro-, nano-and hierarchical structures for superhydrophobicity, self-cleaning and low adhesion. *Philosophical Transactions of the Royal Society A: Mathematical, Physical and Engineering Sciences*, 367(1894):1631–1672, 2009.
28. Pushpapraj Singh, Dhairya Singh Arya, and Udit Jain. Mem-flash non-volatile memory device for high-temperature multibit data storage. *Applied Physics Letters*, 115(4):043501, 2019.
29. Cristiano Palego, Jie Deng, Zhen Peng, Subrata Halder, James CM Hwang, David I Forehand, Derek Scarbrough, Charles L Goldsmith, Ian Johnston, Suresh K Sampath, et al. Robustness of rf mems capacitive switches with molybdenum membranes. *IEEE Transactions on Microwave Theory and Techniques*, 57(12):3262–3269, 2009.
30. Rashed Mahameed and Gabriel M Rebeiz. Rf mems capacitive switches for wide temperature range applications using a standard thin-film process. *IEEE transactions on microwave theory and techniques*, 59(7):1746–1752, 2011.
31. Shahin Siahpour, Mahdi Moghimi Zand, and Mohammad Mousavi. Dynamics and vibrations of particle-sensing mems considering thermal and electrostatic actuation. *Microsystem Technologies*, 24(3):1545–1552, 2018.
32. CH Mastrangelo and CH Hsu. Mechanical stability and adhesion of microstructures under capillary forces. ii. experiments. *Journal of Microelectromechanical systems*, 2(1):44–55, 1993.
33. MP De Boer and TA Michalske. Accurate method for determining adhesion of cantilever beams. *Journal of applied physics*, 86(2):817–827, 1999.
34. Raffaele Ardito, Alberto Corigliano, and Attilio Frangi. Modelling of spontaneous adhesion phenomena in micro-electro-mechanical systems. *European Journal of Mechanics-A/Solids*, 39:144–152, 2013.
35. Raffaele Ardito, Alberto Corigliano, Attilio Frangi, and Francesco Rizzini. Advanced models for the calculation of capillary attraction in axisymmetric configurations. *European Journal of Mechanics-A/Solids*, 47:298–308, 2014.
36. M. Pallay, Ronald Miles, and S. Towfighian. Merging parallel-plate and levitation actuators to enable linearity and tunability in electrostatic mems. *Journal of Applied Physics*, 126(1), 2019.
37. Allen Cowen, Busbee Hardy, Ramaswamy Mahadevan, and Steve Wilcenski. PolyMUMPs Design Handbook a MUMPs® process, 2011.
38. Mohammad Mousavi, Mahdi Moghimi Zand, and Shahin Siahpour. Effect of added mass distribution on the dynamic pi and frequency shifting in mems and nems biosensors. *Microsystem Technologies*, 24(3), 2020.
39. Mohammad I. Younis. *MEMS Linear and Nonlinear Statics and Dynamics*. Wiley, New York, 2008.
40. Arthur Givois, Aurélien Grolet, Olivier Thomas, and Jean-François Deü. On the frequency response computation of geometrically nonlinear flat structures using reduced-order finite element models. *Nonlinear Dynamics*, 97(2):1747–1781, 2019.
41. Dumitru I Caruntu and Ezequiel Juarez. Voltage effect on amplitude–frequency response of parametric resonance of electrostatically actuated double-walled carbon nanotube resonators. *Nonlinear Dynamics*, 98(4):3095–3112, 2019.
42. Fadi M Alsaleem, Mohammad I Younis, and Hassen M Ouakad. On the nonlinear resonances and dynamic pull-in of electrostatically actuated resonators. *Journal of Micromechanics and Microengineering*, 19(4):045013, 2009.